High-Contrast Infrared Absorption Spectroscopy via Mass-Produced Coaxial Zero-Mode Resonators with Sub-10-nm Gaps

Daehan Yoo[1], Daniel A. Mohr[1], Ferran Vidal-Codina[2], Aurelian John-Herpin[3], Minsik Jo[4], Sunghwan Kim[4], Joseph Matson[5], Joshua D. Caldwell[5], Heonsu Jeon[6], Ngoc-Cuong Nguyen[2], Luis Martin-Moreno[7], Jaime Peraire[2], Hatice Altug[3], and Sang-Hyun Oh[1,*]

[1] Department of Electrical and Computer Engineering, University of Minnesota, Minneapolis, Minnesota, 55455, U.S.A.

[2] Department of Aeronautics and Astronautics, Massachusetts Institute of Technology, Cambridge, Massachusetts, 02139, U.S.A.

[3] Institute of BioEngineering, École Polytechnique Fédérale de Lausanne (EPFL), Lausanne 1015, Switzerland

[4] Department of Physics & Department of Energy Systems Research, Ajou University, Suwon 16499, Korea.

[5] Department of Mechanical Engineering, Vanderbilt University, Nashville, TN 37212, U.S.A.

[6] Department of Physics and Astronomy, Seoul National University, Seoul 08826, Korea.

[7] Instituto de Ciencia de Materiales de Aragón and Departamento de Física de la Materia Condensada, CSIC-Universidad de Zaragoza, E-50009 Zaragoza, Spain.

*E-mail: sang@umn.edu

ABSTRACT

We present a wafer-scale array of resonant coaxial nanoapertures as a practical platform for surface-enhanced infrared absorption spectroscopy (SEIRA). Coaxial nanoapertures with gaps as small as 7 nm are fabricated via photolithography, atomic layer deposition of a sacrificial Al_2O_3 layer to define the nanogaps, and planarization via glancing-angle ion milling. At the zeroth-order Fabry-Pérot resonance condition, our coaxial apertures act as a 'zero-mode resonator (ZMR)', efficiently funneling as much as 34% of incident infrared (IR) light along 10-nm annular gaps. After removing Al_2O_3 in the gaps and inserting silk protein, we can couple the intense optical fields of the annular nanogap into the vibrational modes of protein molecules. From 7-nm-gap ZMR devices coated with a 5-nm-thick silk protein film, we observe high-contrast IR absorbance signals drastically suppressing 58% of the transmitted light, and infer a strong IR absorption enhancement factor of 10^4~10^5. These single-nanometer-gap ZMR devices can be mass-produced via batch processing and offer promising routes for broad applications of SEIRA.

KEYWORDS. Coaxial aperture, atomic layer lithography, surface-enhanced infrared absorption (SEIRA), silk protein, extraordinary optical transmission, nanogap.

TOC GRAPHIC

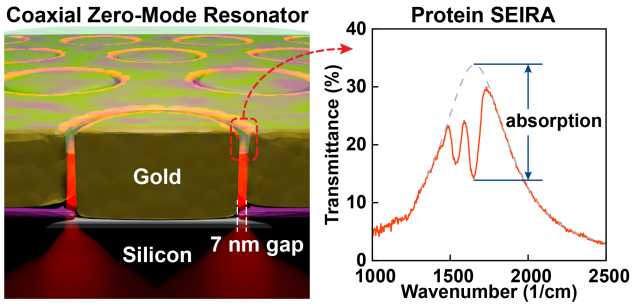

Infrared (IR) spectroscopy has played an important role in various fields of research for nondestructive, label-free detection and identification of specimens via their characteristic IR absorption fingerprints.[1] However, the small absorption cross-sections of molecular vibrations cannot be coupled efficiently to long-wavelength mid-IR radiation, resulting in weak mid-IR absorption signals. The problem is compounded for probing a thin layer of surface-adsorbed molecules such as self-assembled monolayers and biomembranes with mid-IR absorption spectroscopy. One powerful technique to address this challenge is surface-enhanced infrared absorption (SEIRA) spectroscopy,[2-9] which can boost IR absorption of molecules in the vicinity of the metal surface by coupling molecular transitions with tightly confined optical near-fields of surface plasmons[10,11] – density fluctuations of conduction electrons in metals. Similar to the development in the field of surface-enhanced Raman scattering (SERS),[12,13] SEIRA was discovered using roughened metal films,[2] followed by developments of engineered metallic substrates, in particular resonant nanoantennas to efficiently capture mid-IR radiation.[9,14] Various geometries have been used for resonant SEIRA such as gold nanorods,[6,8,15] split-ring resonators,[16] antennas on a mirror,[17,18] and nanogap antennas.[19-21] These technological advances have enabled antenna structures with SEIRA enhancement factors (EF) in the range of 10^4~10^7.[19-21]

While a large fraction of SEIRA research has focused on nanorod antennas, sub-wavelength apertures in metal films have also shown great promise. Recent work compared the SEIRA performance of two complementary structures – gold nanorod and nanoslit.[22] In a nanorod antenna, electromagnetic hotspots exist at the sharp tips, thus only a small number of analyte molecules near the tips contribute to IR absorption, and molecules on the long sidewalls of the nanorod are not efficiently utilized. For that reason, the absolute absorption signal in nanorod

antennas is typically only a few percent or less even though the EF inferred from tip enhancement is very high (>10^4). In a nanoslit (or nanogap) structure, on the other hand, the hot spot is more uniformly distributed along the sidewalls of the slit, leading to stronger overall absorption. Another major difference between them is the degree of field confinement. Typically, mid-IR nanorod antennas exhibit relatively weaker field confinement and larger mode volumes compared with visible-frequency plasmonic resonators.[23] In contrast, the confinement and field enhancement of mid-IR light in a nanogap can improve as its width is decreased even to the single-digit nanometer scale. Indeed, analogous to SERS,[24-27] the largest SEIRA enhancements have been observed from resonant metallic nanogap structures.[21] The key technical challenge to harness SEIRA in the nanogap geometry is to produce long and ultra-narrow gaps and densely pack them over a large area. To this end, many researchers have investigated methods for fabricating IR-resonant nanogap structures via electron-beam lithography,[19] stencil lithography,[28] nanosphere lithography,[29] and thin-film deposition,[21,30-32] among others.

Our approach is based on a technique called atomic layer lithography,[33-35] which has shown the potential to mass-produce resonant single-nanometer gaps. To define ultra-small gaps with high throughput and precision, this technique leverages Angstrom-scale thickness resolution of atomic layer deposition (ALD) to create narrow (down to 1 nm) and long (up to a few centimeters) slits. This method was initially used to create coaxial apertures for SERS applications.[33] Variations of this scheme using adhesive tape[34] and glancing-angle ion milling[35] have been used to create coaxial apertures of diameters ranging from ~100 nm to 50 μm suitable for NIR, MIR, and THz applications. Using this concept, many groups have demonstrated high-throughput production of sub-10 nm gaps, including nanoring cavities,[33-37] long slits for

spectroscopies,[20,38,39] and electrically addressable nanogaps.[40,41] Here we apply this technique to manufacture high-performance SEIRA substrates. As shown previously, the atomic layer lithography process naturally produces annular nanogaps,[33-37] also known as coaxial apertures. A coaxial aperture with sub-micron-sized diameter and sub-10-nm gap typically exhibits its lowest (zeroth) order Fabry-Pérot (FP) resonance in the MIR regime, making this device – coaxial zero-mode resonator (ZMR) – highly effective for resonant SEIRA sensing. We demonstrate wafer-scale production of coaxial ZMR arrays with sub-10-nm gaps. By tuning zero-mode resonances of each coaxial aperture to enable efficient coupling of IR light and vibrational modes of protein molecules in the gap, we obtain unusually intense IR absorbance signals.

For high-throughput batch fabrication, we use a 4-inch undoped (100) silicon wafer as a substrate, which has ~50% transmission in our target mid-IR regime for SEIRA (5-10 μm wavelength) and is compatible with many wafer-scale production tools. For SEIRA sensing of protein absorption bands, the desired diameter of each coaxial aperture is approximately 700 nm, thus the base gold disk patterns can be simply produced over the whole wafer via photolithography (Canon 2500 i3 i-line stepper), electron-beam evaporation of gold (150 nm thickness), and lift-off (Figure 1e). Next, the critical dimension of the coaxial ZMR – gap width – is defined by a conformal coating of Al_2O_3 on gold disk structures via ALD, followed by a second gold sputtering step to produce metal-insulator-metal cavities (Figure 1a). Glancing-angle ion milling shaves the top gold layer to expose Al_2O_3-filled nanogaps (Figure 1b). Al_2O_3 films inside annular nanogaps along the contours of gold disks are removed using H_3PO_4 etchant (Figure 1c). Empty metallic nanogaps are then back-filled with silk fibroin (Figure 1d).

The architecture of our ZMR sensor chip is shown in Figure 1f. A stepper is used to print 157 dies on a 4-inch silicon wafer. Each die (a single SEIRA sensor chip) is designed to operate

over a wide range of mid-IR bands (5 to 10 μm in wavelength) with 20 arrays of coaxial ZMRs with various diameters. Each array is 0.5 mm by 0.5 mm in size and is hexagonally packed with ZMRs (~200,000 per array; ~4 million per die). A scanning electron micrograph (SEM) of a representative array (700 nm diameter, 10 nm gap, 80 nm-thick gold film) is shown in Figure 1g.

Electromagnetic resonances in nanoslits of various types have been studied by many researchers.[42] A rectangular slit in a metal film exhibits a resonance spectrally close to the cutoff frequency determined by the aperture geometries such as slit length and width. Coaxial apertures[43] also possess such cutoff resonances along with higher-order Fabry-Pérot (FP) modes.[44-48] At the cutoff resonance, the real component of the wavevector along the length of the waveguide, k_z, is greatly diminished. Given the general equation for a FP resonance, $2\ h\ k_z = 2\ \pi\ m$, where h is the length of the waveguide and m is the order of the mode, we find that as $k_z \rightarrow 0$, the waveguide can support a zeroth-order FP resonance ($m = 0$), referred to here as the "zero-mode." This zero-mode of a coaxial aperture can exhibit a very long effective wavelength along the cavity (film thickness direction), thus field inside the cavity can constructively interfere independent of the cavity length, h. This phenomenon is analogous to an epsilon-near-zero (ENZ) effect,[49] from which researchers have demonstrated cavity-length-independent resonance, super-coupling, and high transmission through narrow slits. Similar physical principles and framework can also explain the optical properties of coaxial nanoapertures at the zero-mode resonance, where incident mid-IR light can be coupled efficiently into ultra-narrow annular gaps and funneled along, leading to strong field enhancement with the resulting extraordinary optical transmission (EOT).[50] Coaxial apertures have been produced using various techniques.[46,51-53] Our previous work used atomic layer lithography to investigate the properties and tuning of zero-

mode resonances in coaxial apertures with the gap size as small as 2 nm,[35] providing the basis for the present work on SEIRA sensing.

The configuration of a coaxial nanogap array is illustrated in Figure 2b. It should be noted that the zero-mode resonance observed in our sample is a property of the individual rings, not a property of the periodic array or due to inter-ring coupling. Thus the resonance frequency of the zero-mode is determined by the geometries of aperture such as an inner diameter (D_{in}) and gap size (G), rather than the array period (P). This periodicity-independent property of the zero-mode resonance can substantially simplify the ZMR sensor design, thus enabling the high packing density shown in Figures 2f-i. While the array is densely packed with individual ZMR devices, the gaps cover only about 1.8% of the surface. At the zero-mode resonance, however, the measured absolute transmittance is as high as 34% after correcting for the large Fresnel reflections from the high-index silicon substrate (Supporting Information for details).

Numerical simulations of our devices were performed using the finite element method (FEM) with COMSOL Multiphysics. The simulation results for 10-nm-wide coaxial nanogap arrays with four different diameters (Figure 2d) agree well with the measured FTIR spectra (Figure 2e). While we did not explore multi-band SEIRA sensing[54-56] in this work, these results show that it will be possible to mix coaxial apertures with different diameters side-by-side for such applications. Unlike non-zeroth-order FP modes, which show phase variation along the gap, this zero-mode has uniform and strong electric fields inside the entire length of the coaxial nanogap (Figure 2c). As these simulations show, by funneling incident IR radiation through annular nanogaps at the resonance condition, it is possible to create extended ring-shaped hot spots along each aperture and obtain strong electric field |E| enhancement of 100 (Figure 2c).

To use ZMR devices for SEIRA with our fabrication technique, the next step is to remove Al_2O_3 in the high-aspect-ratio nanogap and refill the empty gap with analyte molecules. Efficient removal of Al_2O_3 films in vertical nanogaps can be performed using a H_3PO_4 solution at 60°C, which we found to cause little damage to our nanogap structures. While we cannot measure the etch depth in the gap directly without performing extensive transmission electron microscopy measurements, we can monitor the mid-IR transmission spectra from the same device with increased etching time and compare to computational results to determine the etch depth (Figure 3b). As the etching time is extended and Al_2O_3 is removed, the zero-mode resonance shifts to shorter wavelengths due to the reduction of the mean refractive index. Based on the quantitative agreement between experiment and simulation, we assume that the Al_2O_3 layer inside the metallic nanogap is fully etched after 4 min in H_3PO_4. The measured transmittance through the nanogaps, which is 32% before Al_2O_3 etching, increases even further, up to 41% as the etching time increases. This effect is reproduced accurately in computer simulations (Figure 3b). Furthermore, we calculated the average electric field intensity over the entire coaxial nanogap volume for the different simulated etch cases (inset in Figure 3b). The average electric field inside the gap increases linearly with the etching amount, which we partially attribute to reduced mid-IR absorption in the Al_2O_3 film.

For SEIRA sensing of proteins using coaxial ZMR devices, we used a spin-coating method[57] to fill the gap with silk fibroin molecules. As well as being a promising biomaterial for potential applications in bioelectronics and photonics, silk fibroin is also a convenient model system for SEIRA due to its ease of thickness control by a simple spin-coating method.[8] A 5-nm-thick layer of silk fibroin was spin-coated on ZMR array samples that had been etched for different durations to determine the fill factor of the thin annular gaps with protein. We then fit their FTIR

spectra with Lorentzian curves to estimate the IR absorption by the silk protein and to calculate the absolute absorption (%) as a function of etching time (inset in Figure 3c). Unetched ZMR arrays show an absorption dip of 4.6% after spin-coating a 5-nm silk fibroin on the top surface. The absorption signal jumps from 4.6% to 14.3% after 1 min of Al_2O_3 etching and then increases slowly up to 21% with increased etching time. Since the silk absorption is fairly saturated after 1 min of etching, we expect silk to backfill the gap no more than 25%, i.e. the amount of Al_2O_3 removed from the gap after 1 min etching (Figure 3b).

IR transmission spectra through ZMR devices were measured during the Al_2O_3 etching and after back-filling with silk protein. As shown in Figure 4a and b, after 4 min of Al_2O_3 etching, the zero-mode resonance peak shifts towards shorter wavelengths (higher wavenumbers) while the transmission is increased. The resonance peak then returns to longer wavelengths after the empty gap is partially backfilled with silk fibroin. We measured the mid-IR dielectric constants of our spin-coated silk fibroin sample via ellipsometry (Table S1), and incorporated these results into FEM simulations with varying degrees of silk back-filling (Figure S3). The overall trend in simulated spectra matches experimental observations. We found that silk fibroin filling approximately 20% of the 10-nm gap matches well with our experimentally measured values (Figures 4a and c). To identify which vibrational modes contribute to the absorption dips and to estimate the SEIRA EF, the absorbance ($A= -10^3 \times \log_{10}(T/T_{fit})$) calculated from Figures 4a-b is compared in Figure 4d. From both 7-nm and 10-nm gap ZMR devices, two strong absorbance peaks were observed at 1650 cm^{-1} and 1546 cm^{-1}, which correspond to the representative vibrational modes of amide I and amide II, respectively. These extraordinary absorbance peaks of 378 mOD (58% of transmitted light) measured from only 5-nm-thick silk protein layers are about 15 times stronger than absorbance of 25 mOD measured from nanorod antenna arrays.[8]

Next, we calculate SEIRA enhancement factors defined as $EF = (A_{SEIRA}/V_{SEIRA})/(A_0/V_0)$, where A_{SEIRA} is the enhanced absorbance measured from a ZMR device, A_0 is the absorbance measured from a bare Au film covered with a 5-nm-thick silk film, V_{SEIRA} is the volume of silk fibroin that contributes to IR absorption in ZMR, and V_0 is the volume of silk coated on a bare Au substrate. Based on our FEM modeling shown in the SI, we assume that the silk protein filling only 20% (15%) of 10-nm (7-nm) gap ZMR provides an upper-bound on our EF, while 100% filling provides a lower-bound. To calculate the precise SEIRA detection volume, we separate the effective sensing volume into two regions: "inside coax" and "outside coax". The sensing volume for "inside coax" is simply equal to $\pi (R_{out}^2-R_{in}^2) \times (T_{silk\ inside\ coax})$, where $R_{in,\ out}$ is the inner and outer ring radius, $T_{silk\ inside\ coax}$ is the thickness of nanogap cavity filled with silk fibroin. On the other hand, as shown in Figure 2c, the fringe field over the nanogap should also be considered as the effective sensing volume. We include the volume contribution from this field up to the $1/e$ value of the electric field, which is defined as $\pi[(R_{out}+R_{fringe})^2-(R_{in}- R_{fringe})^2] \times (T_{silk\ outside\ coax})$, where R_{fringe} is the decay length of the electric field from the nanogap, $T_{silk\ outside\ coax}$ is the thickness of silk film spin-coated on the top surface (Supporting information for details). The areal fraction of a coaxial aperture per a unit cell is only ~1.8% for 10 nm gaps (~1.3% for 7 nm gaps). However, the maximum sensing volume fraction in the case of 20% filling is calculated as ~8% in 10-nm gaps (~5.4% in 7-nm gaps) due to the depth of the gap. To measure the absorbance (A_0) of a thin silk film on a reference Au substrate for the EF calculation, infrared reflection absorption spectroscopy (IRRAS) was employed. Detailed IRRAS and SEIRA EF calculations are included in the SI. For a 7-nm ZMR array covered with a 5-nm-thick silk protein layer, a SEIRA EF of 9.6×10^4 is inferred from an Amide I absorbance of 378 mOD with the assumption that 15% of the gap (along the film thickness direction) is filled

with silk fibroin and contributes to the SEIRA signal, while an EF of 2.33×10^4 is calculated if we assume that the entire gap contributes to SEIRA signal. This range of EF values (from 2.33×10^4 to 9.6×10^4) obtained from our coaxial ZMR substrates are consistent with the maximum electric field enhancement ($|E/E_0|^2=2.8\times10^4$) calculated from FEM modeling. Most notably, the unusually high absorbance values and high contrast from our devices result from the high EF combined with background-free transmission measurements, and the precise overlap of protein molecules with the tightly confined mid-IR light funneled along the nanogap.

In summary, we have demonstrated high-contrast SEIRA wherein a 5-nm-thick silk protein layer coated onto our coaxial nanoapertures absorbs as much as 58% of transmitted light at the zero-mode resonance condition in 7-nm annular gaps. Compared with gold nanorod antennas with tip-localized hot spots, extended annular hotspots in our device can more uniformly enhance IR absorption for analyte molecules in and around the gap. Our sub-10-nm coaxial zero mode resonators can be mass-produced on silicon wafers using standard photolithography and ALD, which is an important step towards practical applications of SEIRA.

Supporting information. Methods for computer simulations, device fabrication, optical measurements, experimental normalization procedure, mid-IR dielectric constants of silk fibroin films, and SEIRA EF calculations. This material is available free of charge via the Internet at http://pubs.acs.org.

Author Contributions. D.Y. and S.-H.O. conceived and designed the experiments. D.Y. performed sample fabrication, electron microscopy, and FTIR characterization. D.A.M., F.V.-C., N.-C. N. and J.P. performed numerical simulations. A.J.-H. and H.A. contributed to theoretical analysis. M.J. and S.K. prepared and provided silk fibroin samples. J.M. and J.D.C. performed ellipsometry measurements and dielectric function extraction from the silk fibroin samples. All authors analyzed the data and wrote the paper together.

ACKNOWLEDGMENTS

This research was supported primarily by the U.S. National Science Foundation (ECCS 1610333 to D.Y. and S.-H.O.) and Seagate Technology (D.A.M. and S.-H.O.). D.A.M. acknowledges the National Institutes of Health Biotechnology Training Grant (NIH T32 GM008347). L.M.-M acknowledge financial support by the Spanish MINECO under contract No. MAT2014-53432-C5. F.V.-C., N.C.N. and J.P. acknowledge support from the AFOSR Grant (No. FA9550-11-1-0141 and No. FA9550-12-0357). A.J-H. and H.A. acknowledge European Research Council Consolidator Grant (ERC-2015-CoG-682167). Device fabrication was performed at the Minnesota Nanofabrication Center at the University of Minnesota, which receives partial support from NSF through the National Nanotechnology Coordinated Infrastructure (NNCI). Electron microscopy and FTIR measurements were performed at the Characterization Facility, which has received capital equipment from NSF MRSEC. J.D.C. and J.M. acknowledge Dr. Thomas Tiwald of J.A. Woolam, Inc. for his assistance in fine-tuning the dielectric function fitting.

Notes. The authors declare no competing financial interests.

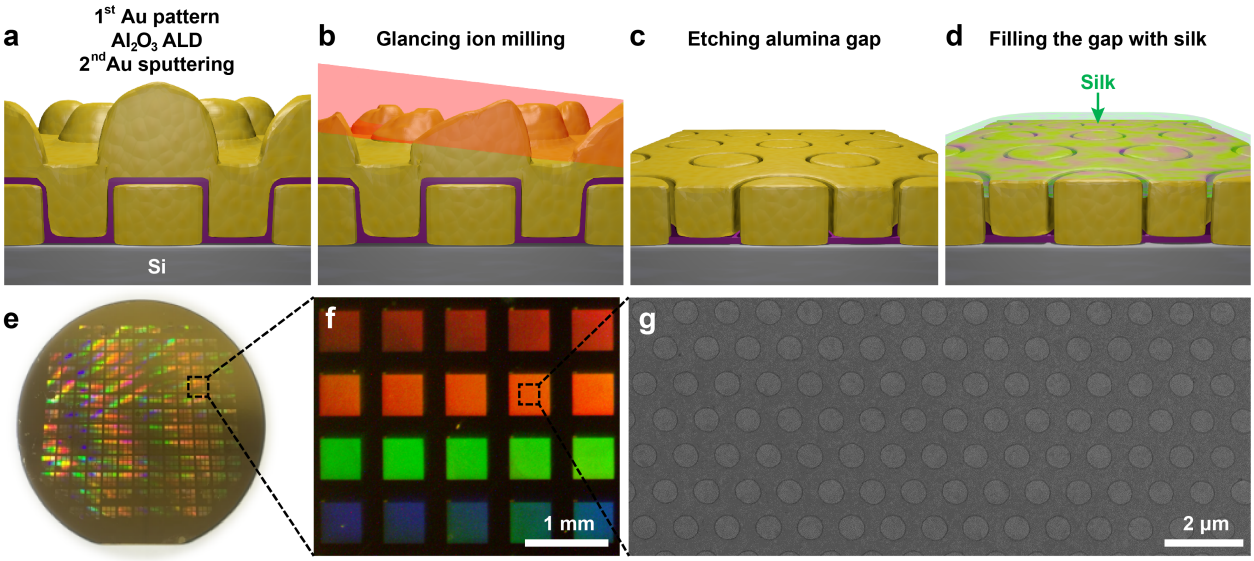

Figure 1. The process flow to mass-produce ZMR chips consisting of coaxial nanoapertures with either 7 nm or 10 nm gaps. (a) First, the Au disk arrays are patterned on the entire 4-inch Si wafer via photolithography, followed by metal evaporation and lift-off. An Al_2O_3 film is then conformally coated on the patterned Au disk array using ALD. The second Au film is sputtered atop of the Al_2O_3-coated Au disk array. (b) Glancing-angle ion milling shaves and polishes the top metal layer, exposing Al_2O_3–filled nanorings. (c) The Al_2O_3 layer inside the nanogap is eliminated using H_3PO_4 etchant and the resulting metallic nanogap becomes accessible to the outside. (d) The metallic nanogap is filled with silk fibroin by spin-coating. (e) Photograph of ZMR sensor arrays on a 4-inch silicon wafer. 4-inch silicon wafer incudes 157 dies. (f) Photograph of 20 arrays of resonant coaxial nanoapertures per die can cover the spectral range of 5-10 μm. Each array is 0.5 mm × 0.5 mm in size (~200,000 rings/ array). (g) SEM image of a dense coaxial nanoaperture array with 10-nm gaps. Scale bars: (f) 1 mm, (g) 2 μm.

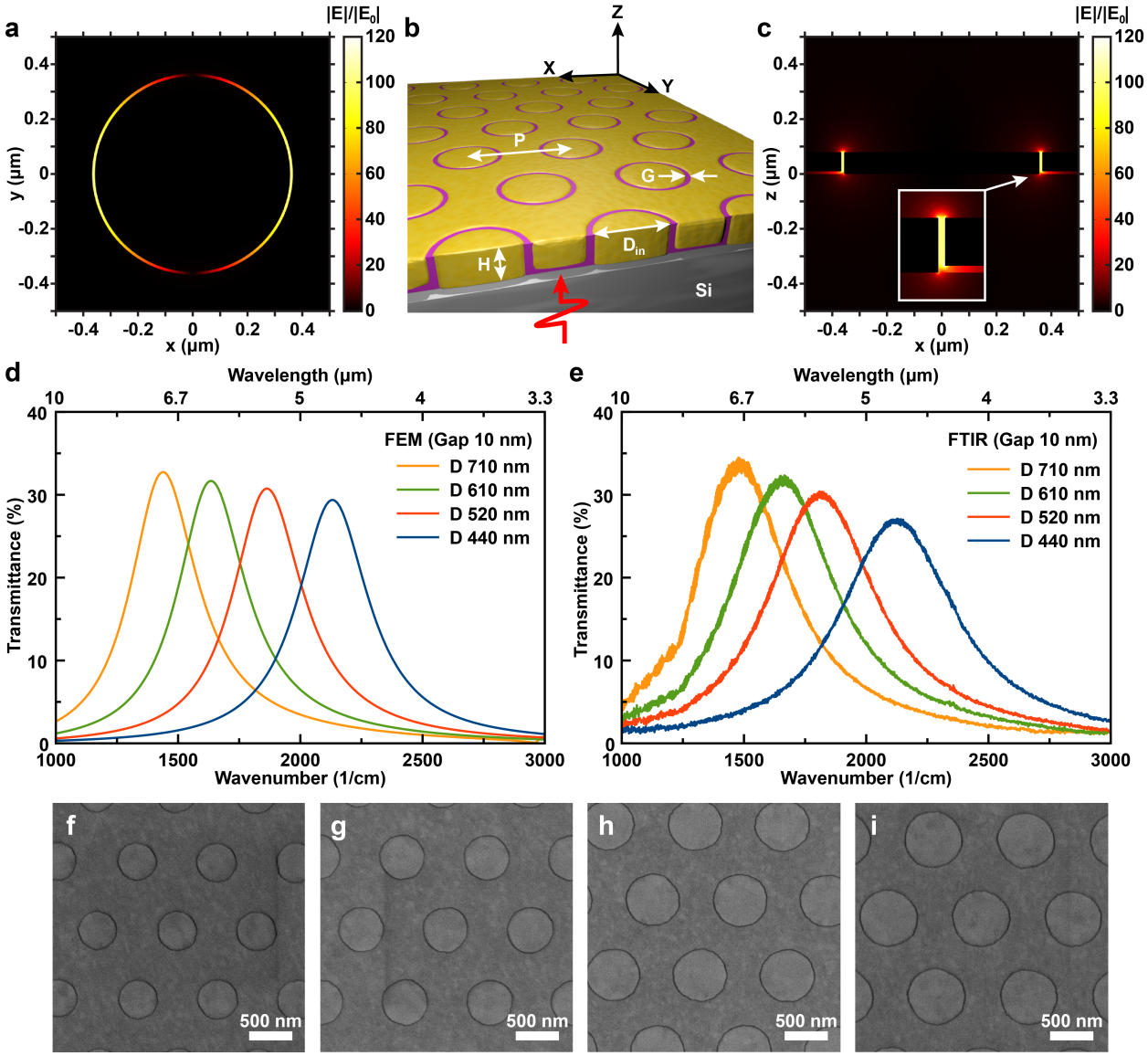

Figure 2. (a) Schematics of a coaxial nanoaperture array on a Si substrate. Horizontal and vertical distributions of electric field in the coaxial nanoaperture with a 10 nm gap (G), 710 nm diameter (D_{in}), and 80 nm thickness (H). Simulations were performed using linearly polarized light launched from a Si substrate. (b) Spectra with different diameters calculated using FEM modeling, (c) Spectra with different diameters measured experimentally using FTIR. (d-g) SEM images of 10-nm-wide coaxial aperture arrays with 440, 520, 610, 710 nm diameters, respectively. Scale bars: (d-g) 500 nm.

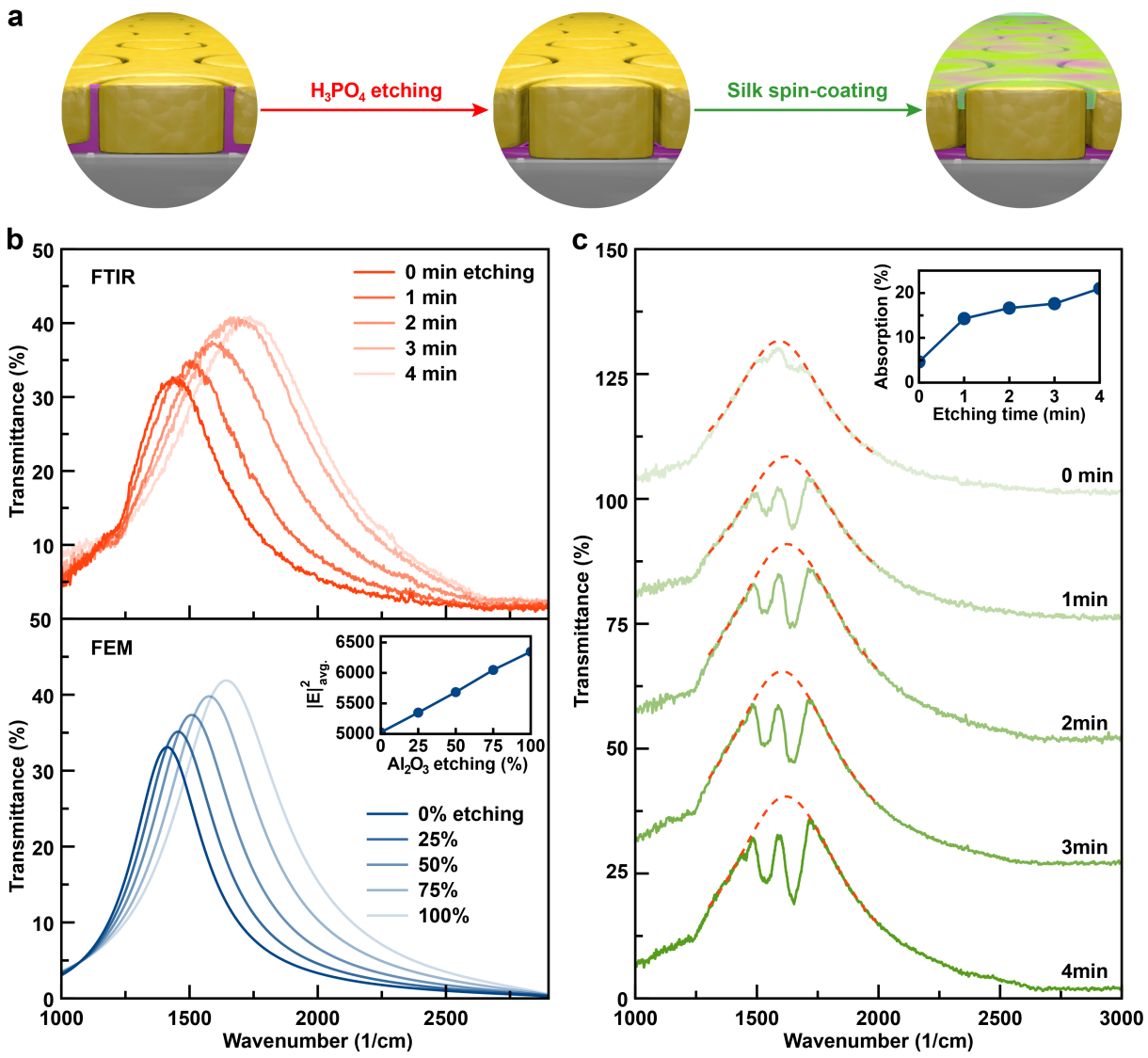

Figure 3. Optical response of coaxial ZMRs with 10-nm gaps to the refractive index change inside the metallic nanogap. (a) Illustration depicts the change the coaxial nanogap goes through during Al_2O_3 etching and silk spin-coating. (b) The cutoff resonance shifts toward shorter wavelengths as the Al_2O_3 etching time increases (upper panel). FEM-simulated cutoff resonances with different portions of air inside the gap (lower panel). Average field intensity enhancement over the whole coaxial nanogap volume is plotted as a function of a percentage of Al_2O_3 etching (inset). (c) Absorption intensity of silk covered on coaxial nanoapertures increases as the Al_2O_3 etching time is extended. Absorption intensity is plotted as a function of the Al_2O_3 etching time (inset).

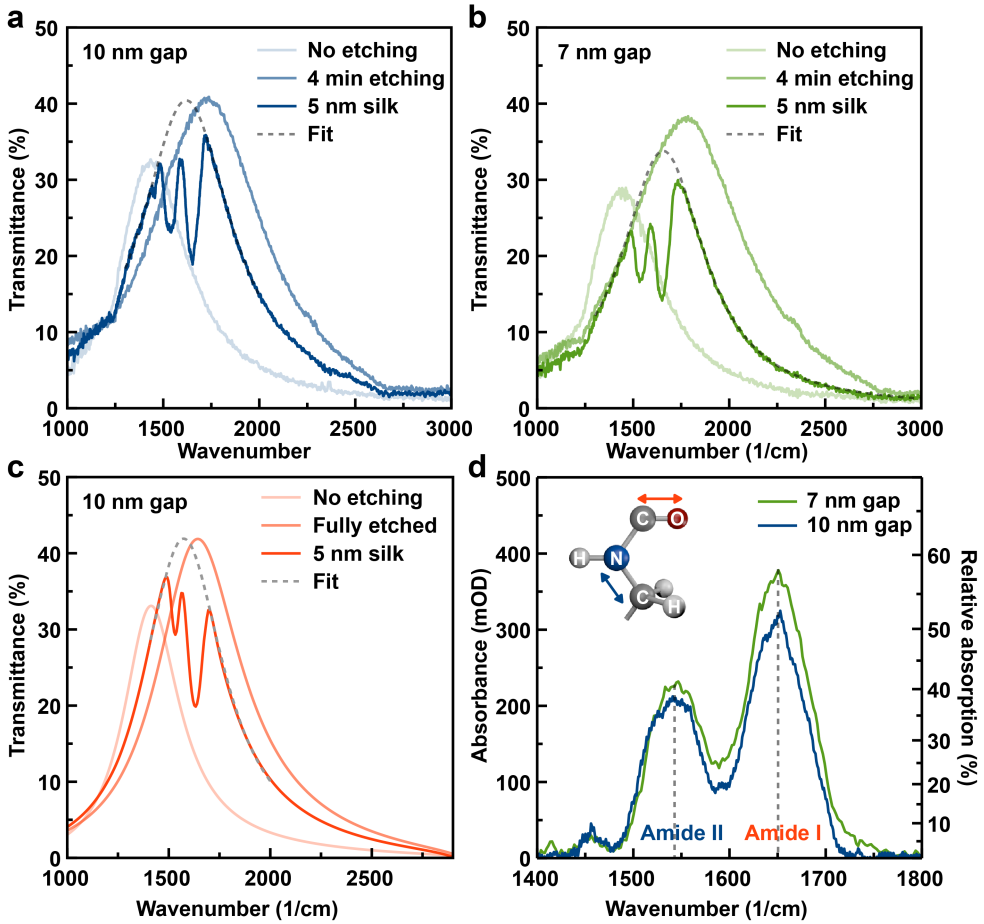

Figure 4. (a) and (b) The comparison of zero-mode resonances measured from 10- and 7-nm-wide coaxial nanoapertures respectively, before Al_2O_3 etching, after Al_2O_3 etching, and after silk spin-coating. (c) The comparison of zero-mode resonances for each step numerically modeled using FEM. (d) Absorbance calculated from (a), (b). They show two distinct absorption signals resulting from the amide I and II bands of protein molecules.

References

(1) Griffiths, P. R.; de Haseth, J. A. *Fourier Transform Infrared Spectrometry*, 2nd ed.; John Wiley & Sons, Inc.: Hoboken, NJ, USA, 2007.

(2) Hartstein, A.; Kirtley, J. R.; Tsang, J. C. *Phys. Rev. Lett.* **1980**, *45*, 201–204.

(3) Osawa, M. *Topics Appl. Phys.* **2001**, *81*, 163–187.

(4) Aroca, R. F.; Ross, D. J.; Domingo, C. *Appl. Spectrosc.* **2004**, *58*, 324A–338A.

(5) Rodriguez, K. R.; Shah, S.; Williams, S. M.; Teeters-Kennedy, S.; Coe, J. V. *J. Chem. Phys.* **2004**, *121*, 8671.

(6) Neubrech, F.; Pucci, A.; Cornelius, T.; Karim, S.; García-Etxarri, A.; Aizpurua, J. *Phys. Rev. Lett.* **2008**, *101*, 157403.

(7) Lal, S.; Grady, N. K.; Kundu, J.; Levin, C. S.; Lassiter, J. B.; Halas, N. J. *Chem. Soc. Rev.* **2008**, *37*, 898–911.

(8) Adato, R.; Yanik, A. A.; Amsden, J. J.; Kaplan, D. L.; Omenetto, F. G.; Hong, M. K.; Erramilli, S.; Altug, H. *Proc. Natl. Acad. Sci. USA* **2009**, *106*, 19227–19232.

(9) Neubrech, F.; Huck, C.; Weber, K.; Pucci, A.; Giessen, H. *Chem. Rev.* **2017**, *117*, 5110–5145.

(10) Ritchie, R. *Phys. Rev.* **1957**, *106*, 874.

(11) Barnes, W. L.; Dereux, A.; Ebbesen, T. W. *Nature* **2003**, *424*, 824–830.

(12) Haynes, C. L.; McFarland, A.; Van Duyne, R. P. *Anal. Chem.* **2005**, *77*, 338A–346A.

(13) Halas, N. J. *Nano Lett.* **2010**, *10*, 3816–3822.

(14) Giannini, V.; Fernández-Domínguez, A. I.; Sonnefraud, Y.; Roschuk, T.; Fernández-García, R.; Maier, S. A. *Small* **2010**, *6*, 2498–2507.

(15) Giannini, V.; Francescato, Y.; Amrania, H.; Phillips, C. C.; Maier, S. A. *Nano Lett.* **2011**, *11*, 2835–2840.

(16) Cubukcu, E.; Zhang, S.; Park, Y.-S.; Bartal, G.; Zhang, X. *Appl. Phys. Lett.* **2009**, *95*, 043113.

(17) Brown, L. V.; Zhao, K.; King, N.; Sobhani, H.; Nordlander, P.; Halas, N. J. *J. Am. Chem. Soc.* **2013**, *135*, 3688–3695.

(18) Brown, L. V.; Yang, X.; Zhao, K.; Zheng, B. Y.; Nordlander, P.; Halas, N. J. *Nano Lett.* **2015**, *15*, 1272–1280.

(19) Huck, C.; Neubrech, F.; Vogt, J.; Toma, A.; Gerbert, D.; Katzmann, J.; Härtling, T.; Pucci, A. *ACS Nano* **2014**, *8*, 4908–4914.

(20) Chen, X.; Ciracì, C.; Smith, D. R.; Oh, S.-H. *Nano Lett.* **2015**, *15*, 107–113.

(21) Dong, L.; Yang, X.; Zhang, C.; Cerjan, B.; Zhou, L.; Tseng, M. L.; Zhang, Y.; Alabastri, A.; Nordlander, P.; Halas, N. J. *Nano Lett.* **2017**, *17*, 5768–5774.

(22) Huck, C.; Vogt, J.; Sendner, M.; Hengstler, D.; Neubrech, F.; Pucci, A. *ACS Photonics* **2015**, *2*, 1489–1497.

(23) Law, S.; Podolskiy, V.; Wasserman, D. *Nanophotonics* **2013**, *2*, 103–130.

(24) Xu, H.; Bjerneld, E.; Käll, M.; Borjesson, L. *Phys. Rev. Lett.* **1999**, *83*, 4357–4360.

(25) Michaels, A. M.; Jiang, J.; Brus, L. *J. Phys. Chem. B* **2000**, *104*, 11965–11971.

(26) Ward, D. R.; Grady, N. K.; Levin, C. S.; Halas, N. J.; Wu, Y.; Nordlander, P.; Natelson, D. *Nano Lett.* **2007**, *7*, 1396–1400.

(27) Wang, H.; Levin, C. S.; Halas, N. J. *J. Am. Chem. Soc.* **2005**, *127*, 14992–14993.

(28) Aksu, S.; Yanik, A. A.; Adato, R.; Artar, A.; Huang, M.; Altug, H. *Nano Lett.* **2010**, *10*, 2511–2518.

(29) Le, F.; Brandl, D. W.; Urzhumov, Y. A.; Wang, H.; Kundu, J.; Halas, N. J.; Aizpurua, J.; Nordlander, P. *ACS Nano* **2008**, *2*, 707–718.

(30) Miyazaki, H. T.; Kurokawa, Y. *Phys. Rev. Lett.* **2006**, *96*, 097401.

(31) Miyazaki, H. T.; Kurokawa, Y. *Appl. Phys. Lett.* **2006**, *89*, 211126.

(32) Cetin, A. E.; Aksu, S.; Turkmen, M.; Etezadi, D.; Altug, H. *J. Electromagnet. Wave.* **2015**, *29*, 1686–1698.

(33) Im, H.; Bantz, K. C.; Lindquist, N. C.; Haynes, C. L.; Oh, S.-H. *Nano Lett.* **2010**, *10*, 2231–2236.

(34) Chen, X.; Park, H.-R.; Pelton, M.; Piao, X.; Lindquist, N. C.; Im, H.; Kim, Y. J.; Ahn, J. S.; Ahn, K. J.; Park, N.; Kim, D.-S.; Oh, S.-H. *Nature Commun.* **2013**, *4*, 2361.

(35) Yoo, D.; Nguyen, N.-C.; Martín-Moreno, L.; Mohr, D. A.; Carretero-Palacios, S.; Shaver, J.; Peraire, J.; Ebbesen, T. W.; Oh, S.-H. *Nano Lett.* **2016**, *16*, 2040–2046.

(36) Im, H.; Bantz, K. C.; Lee, S. H.; Johnson, T. W.; Haynes, C. L.; Oh, S.-H. *Adv. Mater.* **2013**, *25*, 2678–2685.

(37) Park, H.-R.; Chen, X.; Nguyen, N.-C.; Peraire, J.; Oh, S.-H. *ACS Photonics* **2015**, *2*, 417–424.

(38) Chen, X.; Park, H.-R.; Lindquist, N. C.; Shaver, J.; Pelton, M.; Oh, S.-H. *Sci. Rep.* **2014**, *4*, 6722.

(39) Chen, X.; Lindquist, N. C.; Klemme, D. J.; Nagpal, P.; Norris, D. J.; Oh, S.-H. *Nano Lett.* **2016**, *16*, 7849–7856.

(40) Cui, A.; Liu, Z.; Dong, H.; Yang, F.; Zhen, Y.; Li, W.; Li, J.; Gu, C.; Zhang, X.; Li, R.; Hu, W. *Adv. Mater.* **2016**, *28*, 8227–8233.

(41) Barik, A.; Chen, X.; Oh, S.-H. *Nano Lett.* **2016**, *16*, 6317–6324.

(42) García-Vidal, F. J.; Martín-Moreno, L.; Ebbesen, T. W.; Kuipers, L. *Rev. Mod. Phys.* **2010**, *82*, 729–787.

(43) Baida, F. I.; Van Labeke, D. *Opt. Commun.* **2002**, *209*, 17–22.

(44) Yanik, A. A.; Wang, X.; Erramilli, S.; Hong, M. K.; Altug, H. *Appl. Phys. Lett.* **2008**, *93*, 081104.

(45) Catrysse, P. B.; Fan, S. *Appl. Phys. Lett.* **2009**, *94*, 231111.

(46) de Waele, R.; Burgos, S. P.; Polman, A.; Atwater, H. A. *Nano Lett.* **2009**, *9*, 2832–2837.

(47) Li, D.; Gordon, R. *Phys. Rev. A* **2010**, *82*, 041801(R).

(48) Saleh, A. A. E.; Dionne, J. A. *Nano Lett.* **2012**, *12*, 5581–5586.

(49) Edwards, B.; Alù, A.; Young, M. E.; Silveirinha, M.; Engheta, N. *Phys. Rev. Lett.* **2008**, *100*, 033903.

(50) Ebbesen, T. W.; Lezec, H. J.; Ghaemi, H. F.; Thio, T.; Wolff, P. *Nature* **1998**, *391*, 667–669.

(51) Fan, W.; Zhang, S.; Minhas, B.; Malloy, K. J.; Brueck, S. R. J. *Phys. Rev. Lett.* **2005**, *94*, 033902.

(52) Poujet, Y.; Salvi, J.; Baida, F. I. *Opt. Lett.* **2007**, *32*, 2942–2944.

(53) Melli, M.; Polyakov, A.; Gargas, D.; Huynh, C.; Scipioni, L.; Bao, W.; Ogletree, D. F.; Schuck, P. J.; Cabrini, S.; Weber-Bargioni, A. *Nano Lett.* **2013**, *13*, 2687–2691.

(54) Aouani, H.; Šípová, H.; Rahmani, M.; Navarro-Cia, M.; Hegnerová, K.; Homola, J.; Hong, M.; Maier, S. A. *ACS Nano* **2013**, *7*, 669–675.

(55) Rodrigo, D.; Limaj, O.; Janner, D.; Etezadi, D.; de Abajo, F. J. G.; Pruneri, V.; Altug, H. *Science* **2015**, *349*, 165–168.

(56) Limaj, O.; Etezadi, D.; Wittenberg, N. J.; Rodrigo, D.; Yoo, D.; Oh, S.-H.; Altug, H. *Nano Lett.* **2016**, *16*, 1502–1508.

(57) Lee, M.; Jeon, H.; Kim, S. *Nano Lett.* **2015**, *15*, 3358–3363.